

Standoff detection of hidden objects using backscattered ultra-intense laser-produced x-rays

H. Kuwabara, Y. Mori, and Y. Kitagawa

Citation: [Journal of Applied Physics](#) **114**, 083103 (2013); doi: 10.1063/1.4819084

View online: <http://dx.doi.org/10.1063/1.4819084>

View Table of Contents: <http://scitation.aip.org/content/aip/journal/jap/114/8?ver=pdfcov>

Published by the [AIP Publishing](#)

Articles you may be interested in

[Void detection in copper interconnects using energy dispersive x-ray spectroscopy](#)

J. Vac. Sci. Technol. B **30**, 051803 (2012); 10.1116/1.4742855

[Sub-MeV tunably polarized X-ray production with laser Thomson backscattering](#)

Rev. Sci. Instrum. **79**, 053302 (2008); 10.1063/1.2931010

[High resolution hard x-ray spectroscopy of femtosecond laser-produced plasmas with a CZT detector](#)


Rev. Sci. Instrum. **74**, 5035 (2003); 10.1063/1.1628824

[Elemental analysis using hard x-ray emission from a laser-produced plasma, induced by a femtosecond laser pulse](#)

Rev. Sci. Instrum. **72**, 3940 (2001); 10.1063/1.1405790

[Studies of ultrafast laser-produced X-ray sources](#)

AIP Conf. Proc. **443**, 92 (1998); 10.1063/1.56560


The Shimadzu logo, consisting of a stylized 'S' inside a circle, is positioned to the left of the company name.**SHIMADZU**
Excellence in Science

Powerful, Multi-functional UV-Vis-NIR and FTIR Spectrophotometers

Providing the utmost in sensitivity, accuracy and resolution for applications in materials characterization and nano research

- Photovoltaics
- Polymers
- Thin films
- Paints
- Ceramics
- DNA film structures
- Coatings
- Packaging materials

[Click here to learn more](#)

A row of four Shimadzu spectrophotometers is shown. From left to right: a small, compact model; a larger model with a sample compartment open; a large, boxy model with a control panel; and a tall, vertical model with a large sample area.

Standoff detection of hidden objects using backscattered ultra-intense laser-produced x-rays

H. Kuwabara,¹ Y. Mori,^{2,a)} and Y. Kitagawa²

¹IHI Corporation, 1, Shin-Nakahara-cho, Isogo-ku, Yokohama 235-8501, Japan

²The Graduate School for the Creation of New Photonics Industries, 1955-1 Kurematsucho, Nishiku, Hamamatsu, Shizuoka 431-1202, Japan

(Received 30 May 2013; accepted 6 August 2013; published online 22 August 2013)

Ultra-intense laser-produced sub-ps X-ray pulses can detect backscattered signals from objects hidden in aluminium containers. Coincident measurements using primary X-rays enable differentiation among acrylic, copper, and lead blocks inside the container. Backscattering reveals the shapes of the objects, while their material composition can be identified from the modification methods of the energy spectra of backscattered X-ray beams. This achievement is an important step toward more effective homeland security. © 2013 Author(s). All article content, except where otherwise noted, is licensed under a Creative Commons Attribution 3.0 Unported License. [<http://dx.doi.org/10.1063/1.4819084>]

I. INTRODUCTION

Scattering from ultra-intense laser-produced X-rays is expected to be a very useful non-destructive diagnostic tool because of its potential of high spatial resolution^{1–6} and its ability to identify objects in hard-to-reach spaces.⁷ We propose this source for performing standoff inspection of hidden objects. Maintaining the safety of public transport facilities, such as airports and seaports, is a serious concern for national security. Security guards and inspectors must also be protected from potential dangers. Inspection protocols demand that both source and sensor be located on the same side of the inspected object, and for their safety, they must be at least 10 m from the object.

Backscattered X-ray inspection is the only technique that meets such requirements. However, because both incident and backscattered X-ray beam intensities decrease inversely with distance, current X-ray tubes provide a stand-off distance of only 1.5 m.⁸ This complicates detecting sufficient backscattered signals that exceed the natural radiation in the environment.⁹ However, using a more powerful source would endanger the environment. Thus, backscattering can currently be used only in a combined inspection system.¹⁰

These problems, however, can be resolved by using a pulsed X-ray source as it would enable us to capture weak yet significant pulses in a narrow window coincident with the incident pulse. An ultra-intense laser produces extremely short (<1 ps) X-ray pulses, thereby reducing sampled natural radiation to the level of zero counts. Such a laser would be portable in the future. Furthermore, since it provides a very small spot source of less than a few hundred micrometres, it is environmentally safe.

In a previous study, on backscattered X-ray standoff inspection using laser-produced X-ray pulses,¹¹ we demonstrated that when objects are arrayed side by side, backscattered X-rays can reconstruct the array image. Extremely short X-ray pulse measurement has the advantage of

detecting very weak backscattered signals by the coincident measurement technique.

We report here that X-ray backscattering can identify the shapes of objects hidden in an aluminium container, even with photon-counting-level signals. Coincident measurements using primary X-rays enable differentiation among acrylic, copper, and lead blocks inside the container. A simple calculation using the Klein and Nishina formula reproduces the backscattered images of the objects. In addition, the objects modify the energy spectra of the backscattered X-rays, which can further confirm their identities.

II. EXPERIMENTAL SETUP AND RESULTS

Figure 1 shows the setup for experiments on backward imaging. A 1.2-TW tabletop Ti:Sapphire chirped pulse amplification (CPA) laser¹² is focused on a thin foil, generating Bremsstrahlung X-rays at 10 Hz. The laser has a wavelength of 800 nm, pulse width of 200 fs, and energy of 62 mJ. The beam is focused using a 138-mm focal length (f/3.9) off-axial parabola on a 0.5-mm-thick aluminium target incident at 30° (p-polarization) in a stainless-steel vacuum chamber with a diameter of 80 cm.¹¹

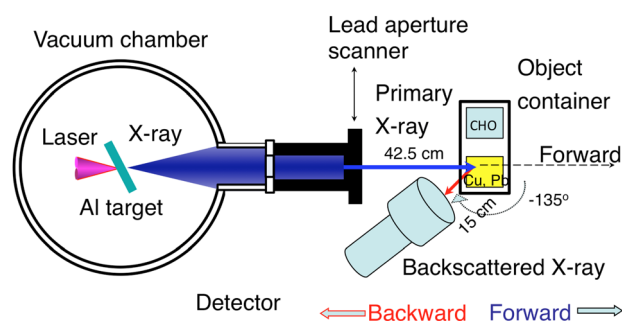


FIG. 1. Setup for backward imaging experiments. A laser (left) generating picosecond pulsed X-rays in the vacuum chamber is focused on an aluminium target. The X-rays penetrate the vacuum window and travel through a movable lead collimator (centre) to scan objects in the aluminium container (right). Backscattered X-rays reach the scintillation detector (centre, bottom).

^{a)}Electronic mail: ymori@gpi.ac.jp

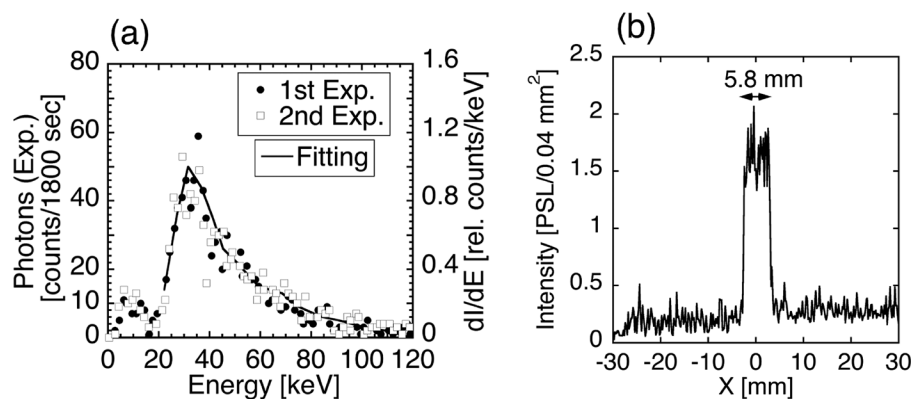


FIG. 2. (a) Primary X-ray spectrum. The solid curve is the fitted spectrum. (b) Beam profile of the primary X-rays.

The target moves during the shot interval with a velocity of $50 \mu\text{m/s}$, which allows irradiation for a few minutes, or 1000 shots. The laser spot size is $8 \mu\text{m}$. The focal intensity I is $6.2 \times 10^{17} \text{ W/cm}^2$, which accelerates electrons on the target surface to an energy produced by the photon pressure $[(1 + I/(1.37 \times 10^{18}))^{1/2} - 1] \times 511 \sim 104 \text{ keV}$.¹³ The accelerated electrons pass through the target and emit Bremsstrahlung X-rays with energies of up to a 100 keV at the corresponding laser pulse duration. The X-rays are extracted through a vacuum window¹¹ and supplied for the experiments as a primary X-ray beam.

Figure 2(a) shows the primary X-ray spectrum taken by a CdTe X-ray detector (XR-100T, Amptek, Inc.) operating in a photon-counting mode. The X-rays below 20 keV are attenuated by the 5-mm-thick BK7 vacuum window, resulting in the peak near 40 keV. Laser-produced source X-rays have divergence larger than 0.7π rad.¹⁴ Thus, we shape and scan primary X-ray beams for backscattering experiments, as shown in Fig. 1. The X-rays are passed through a lead collimator placed 90 cm from the source; these X-rays are capable of scanning an object at 132.5 cm. The collimator is made of 50-mm-thick lead blocks and has a 5-mm-wide and 100-mm-high aperture that focuses the beam into a rectangle. The resulting collimated X-ray has a beam width of 5.8 mm, as shown in Fig. 2(b) and an estimated divergence of 1.4 mrad at the surface of the object. The attenuation length of X-rays in air at normal conditions is $9.4 \times 10^{-4} \text{ cm}^{-1}$ for 20 keV and $1.8 \times 10^{-4} \text{ cm}^{-1}$ for 100 keV.¹⁵ In these experiments, the travelling distance of X-rays is around 1 m, so we can disregard any attenuation of produced X-rays in air.

Figure 3 shows the container and its contents, which are a block of acrylic resin and another block of either copper or

lead. An object inside the container scatters most of the beam forward, but a fraction, occasionally on the order of a single photon, travels backward. To scan an object, we sweep the collimator transversely to the beam line, as shown in Fig. 1. The detector is a fast plastic scintillator (BC-404, Saint Gobain K.K.) with a diameter of 90 mm and thickness of 100 mm, coupled to a photomultiplier (H8443, Hamamatsu photonics K.K.). A 2-mm-thick lead shield covers both object and detector to prevent laser-produced X-ray leakage from vacuum chamber ports, as reported previously.¹¹ It is set at -135° to the incident beam and 15 cm from the object. The laser pulse frequency is 10 Hz.

For coincident measurements, a 1-GHz digital oscilloscope (DP07104, Tektronics, Inc.) detects the backscattered signals only when they pass through a 200-ns window triggered by the laser pulse.

Coincident measurements using primary X-rays allow a backside scintillation detector to detect a backscattered signal of even a single photon without loss due to natural radiation noise.¹⁶ We measured natural radiation using the same scintillator system. The scintillator counted 12 natural X-ray beams in 10 ms without any lead shielding, so a time interval of less than a few hundred nanoseconds is sufficiently short to reduce natural noise to the zero-count level. Even when we lengthened the detection time to 500 s, the coincident measurement detected no natural noise. This confirms that coincident measurement is essential for reducing the effects of natural radiation. The lead shield, containing the objects and X-ray detector, prevents X-ray leakage from the laser irradiation chamber, as mentioned above. We stress that the coincident measurement, and not the lead shield, suppresses noise due to natural radiation. The pulse length of the laser-produced X-ray is supposed to be within a few picoseconds.

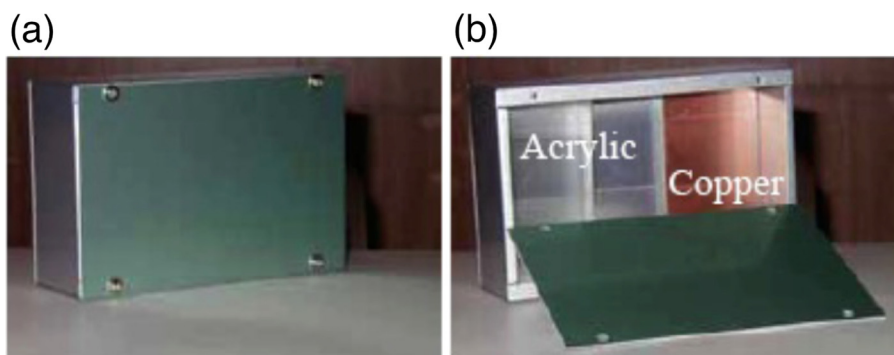


FIG. 3. (a) Aluminium container (0.8-mm thick) in which the objects are hidden. The container dimension is $150 \text{ mm} \times 100 \text{ mm} \times 50 \text{ mm}$. (b) Inside the container are a 30-mm-thick acrylic resin block (left) and a block of either 5-mm-thick copper or 1-mm-thick lead (right).

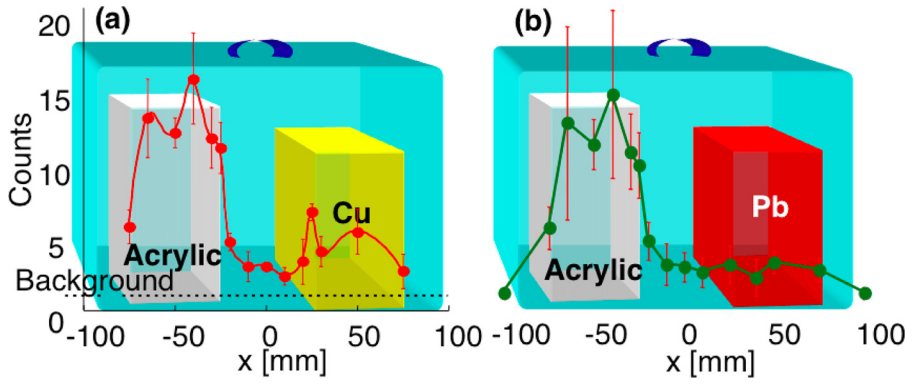


FIG. 4. Backscattered X-ray images show the inside of the container for (a) acrylic resin (left) and copper (Cu, right) and (b) acrylic resin (left) and lead (Pb, right). The horizontal dotted line in (a) gives the level of background noise (1 count). One measured point was obtained from 1000 shots over a 100-s interval. To confirm the data, we repeated these shots three times for case (a) and five times for case (b).

The decay constant of the scintillator is about 1.8 ns. The rising time of the photomultiplier tube H8443 is 1.6 ns. Thus, the overall time resolution of the detector system is about 10 ns, so we set the coincident interval to 200 ns.

We swept the incident beam transversely on the container surface. The incident photons on the container measure about 1000 counts in 100 s. As shown in Figs. 3(a) and 3(b), backscattering detects the objects hidden inside the container, even though the detected photons measure only 15 counts for acrylic resin, 5 for copper, and 2 for lead. The background, shown as the horizontal dashed line in Fig. 4(a), is 1 count, close to the scattering level without the container. Without the coincidence technique, the backscattered signals will be masked by natural radiation. In the figure, the left-hand boundaries of each object show small but sharp peaks: $x = -70$ mm for acrylic in Figs. 4(a) and 4(b), $x = +25$ mm for copper in Fig. 4(a), and $x = +25$ mm for lead in Fig. 4(b). These features probably appear because the primary incident X-rays were not normal to the objects but tilted slightly to the right. Three repeated scans yielded the vertical error bars in Fig. 4(a) and five yielded those in Fig. 4(b). The primary beam shape provided a horizontal resolution of 5.8 mm. Note that the scattering inside an object is attenuated again by the same object. The deeper the point of scattering, higher is the attenuation of backscattering. Furthermore, for a low- Z material, such as acrylic, attenuation is small and hence the backscattered yield is almost proportional to the thickness of the scattering object. But for a high- Z material, such as lead, attenuation is high. Thus, we consider that yield is larger for low- Z materials.

III. MODEL CALCULATIONS

To explain the above experiments, we constructed a one-dimensional slab model of X-ray Compton scattering and attenuation in the scattering materials.¹⁷ Using the Klein and Nishina formula,¹⁸ we calculated probabilities for X-ray-electron scattering. These probabilities are accumulated along the depth of the scattering material, i.e., backscattering from the front and rear surfaces of the case as well as the inner object. Figure 5 shows the schematics of the model. A primary X-ray beam from the source with an energy E and spectrum $dI(E)/dE$ is attenuated by a factor T_{in} to reach the depth z in the target. At that scattering depth, bulk electrons in the target with electron densities $N_e(z)$ scatter those

X-rays to the energy E' towards a scattering angle ϕ into a small angle $d\Omega$ with probability P . These scattered X-rays are attenuated by a factor T_{out} before arriving at the detector. Therefore, the backscattered photon spectrum from z into $d\Omega$, $dI_{out}(E, z)/dE/d\Omega$ is given by

$$\frac{dI_{out}(E, z)}{dE d\Omega} = \frac{dI(E)}{dE} T_{in} P T_{out}, \quad (1)$$

where

$$T_{in}(z, E) = \exp \left[- \int_{z_0}^z \mu(z, E) dz \right], \quad (2)$$

$$P(z, E \rightarrow E', \phi, d\Omega) = \frac{d\sigma(E, \phi)}{d\Omega} N_e(z) dz, \quad (3)$$

$$T_{out}(z, E', \phi) = \exp \left[- \int_{z_0}^z \frac{-\mu(z, E')}{\cos \phi} dz \right]. \quad (4)$$

In these equations, $\mu(z, E)$ is the attenuation coefficient of the target material, z_0 and z_1 are the front and rear depths in the target, respectively. $d\sigma(E, \phi)/d\Omega$ is the differential cross section of photons scattered from a single free electron, as per Klein–Nishina. Here, the attenuation coefficient involves every attenuation processes, including Rayleigh scattering and photoelectric absorption. The primary X-ray energy E and the backscattered X-ray energy E' are related by the Compton scattering formula

$$\frac{E}{E'} = 1 + \frac{E(1 - \cos \phi)}{m_e c^2}. \quad (5)$$

The total backscattered intensity I_{out} captured by the detector within a solid angle $\Delta\Omega$ is obtained by integrating Eq. (1) over depth, energy, and solid angle as shown below

$$\begin{aligned} I_{out} &= \int_{\Delta\Omega} \int_0^\infty \int_{z_0}^{z_1} \frac{dI_{out}(E, z)}{dE d\Omega} dE dz d\Omega = \int_0^\infty \frac{dI(E)}{dE} Q(E) dE \\ &= \int_0^\infty \frac{dI'(E)}{dE} dE. \end{aligned} \quad (6)$$

In Eq. (6), we integrate only over the depth and the solid angle and obtain the backscattered X-ray spectrum shift $Q(E)$ relative to the primary X-ray spectrum as follows:

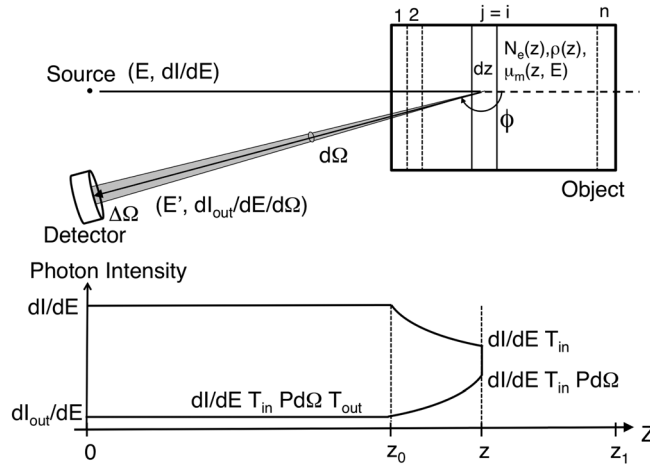


FIG. 5. Calculation model of one-dimensional backscattering photon intensity. Top: The X-ray source and detector are located on the same side of the object, which is composed of n slabs. Bottom: The source X-ray beam enters the target at z_0 and is backscattered at depth z . Over the distance $z-z_0$, both the source and backscattered beams are attenuated by the target. The position z_1 marks the back of the object.

$$Q(E) = \Delta\Omega \frac{d\sigma(E, \phi)}{d\Omega} \times \int_{z_0}^{z_1} e^{-\int_{z_0}^z \left\{ \mu(z, E) - \frac{\mu(z, E')}{\cos\phi} \right\} dz} N_e(z) dz. \quad (7)$$

In this model, the object consists of n slabs; thus, integration over the target thickness can be converted into a sum over thin-slab structures as shown

$$Q(E) = \Delta\Omega \frac{d\sigma(E, \phi)}{d\Omega} \sum_{j=1}^n e^{-\sum_{i=0}^{j-1} \alpha_i t_i} \frac{N_{e,i}}{\alpha_i} [1 - e^{-\alpha_i t_i}], \quad (8)$$

$$\alpha_i \equiv \mu_i(z, E) - \frac{\mu_i(z, E')}{\cos\phi}, \quad \alpha_0 = 0.$$

Here, $N_{e,i}$, t_i , and $\mu_i(z, E')$ are the electron density, thickness, and attenuation coefficient of the i th slab structure, respectively. Since $Q(E)$ is independent of the primary X-ray spectrum $dl(E)/dE$, we obtain the spectral shift. This shift depends on the target materials and its thickness.

We apply this model to the objects hidden in the aluminum container. The object is composed of three slabs ($n=3$); the container's front and rear surface (aluminium) and the inside object (acrylic, copper, or lead). The attenuation coefficient $\mu(z, E) = \rho(z)\mu_m(z, E)$ is evaluated from the material densities $\rho(z)$ and the mass attenuation coefficients $\mu_m(z, E)$.¹⁵

Figure 6 represents the comparison of experimental results with the model calculations, whose curves are relative values. The experimental results (solid circles) are in good agreement with the calculated results (dashed lines), except for small discrepancies for copper (Fig. 6(a)) and lead (Fig. 6(b)). In the experimental data, larger uncertainties occur at the edges of the target slabs. There are two reasons for such uncertainties: (1) the detector and the primary X-ray beam were off-axis by 45° and (2) the detector distance from the object was comparable to object size. In such configurations, for modelling edges or boundaries, the geometry of the object should be taken into account. Nevertheless, in future applications of standoff detection, the source and detector would be on-axis and the distance between source/detector and object would be much larger than the object size. Therefore, rather than the present situation, a 1D model would be valid.

A low- Z object does not significantly attenuate the incident X-ray, so backscattering is almost proportional to the electron density of the object, resulting in higher backscattering yields for higher densities. In contrast, for a high- Z object, attenuation rapidly decreases backscattering, resulting in higher backscattering yields for lower densities. Thus, backscattering increases with density and decreases with Z number of the object. The present study compares experimental results with model calculations; in the future, we would like to compare experimental results with Monte Carlo simulations.

In general, the data in Fig. 4 are, by themselves, not enough to determine the object materials. To do so precisely, we require further information. Figure 7 shows that the scattering materials shifted the energy spectra of the backscattered X-rays, $dl'(E)/dE$. The solid circles represent experimental data and the dashed curves were calculated from Eq. (8) assuming the primary X-ray spectrum shown in

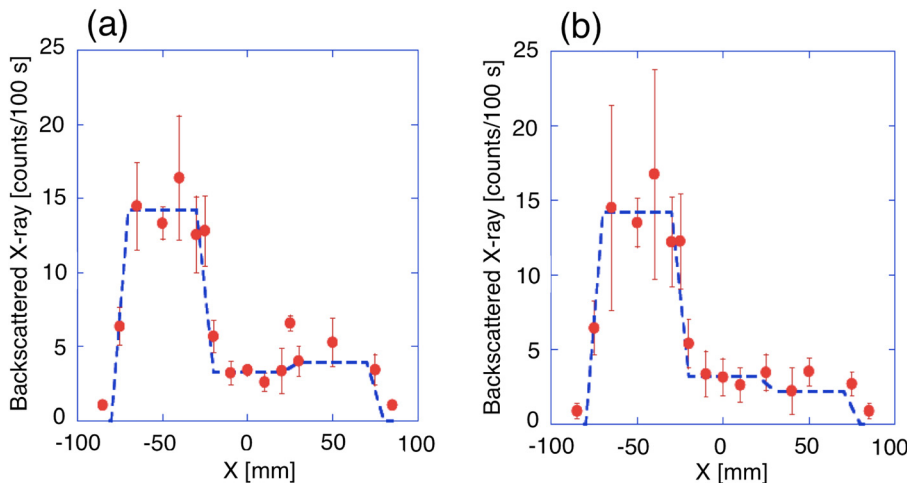


FIG. 6. Comparison of experimental results with model calculations. Solid circle: experimental data from Figs. 4(a) and 4(b). Dashed line: calculations: (a) acrylic and copper; (b) acrylic and lead. In (a) and (b), plateaus between 70 and 25 mm are from acrylic. In (a), plateau between approximately and mm is from Cu. In (b), plateau between approximately and mm is from Pb.

Fig. 2(a). In the experiments, we find that the higher the Z number of the material, the greater the shift in the backscattered peak compared with the primary peak. The calculations reproduce the backscattered X-ray spectrum for low- Z materials, as shown in Figs. 7(a) and 7(b). For copper (Fig. 7(c)), broadening of the backscattered spectrum width is observed in the experiments and their calculations. For lead (Fig. 7(d)), a shift in spectral peak was observed between the calculated and measured curves. This suggests that further detailed spectral measurements are required to identify high- Z materials. In addition, for analysis of high- Z material, we require further actions, such as model improvement. Use of the Monte Carlo method might also improve the agreement between experiments and the model.

Backscattering here is mainly due to photon-electron scattering on the object body. Hence, energy changes in the X-ray photons depend on neither the Z number nor the electron density of the object for individual scattered photons. The spectrum of the backscattered X-ray is thus modified from the incidence spectrum. The spectral shift is small for low- Z materials, such as acrylic resin, or when the container is empty and is large for high- Z materials, such as copper or lead. Hence, combining spectral shifts with backscattering counts provides precise information about the object composition. Therefore, it is necessary to perform coincident measurements, i.e., simultaneous measurements of both primary and scattered signals.

IV. DISCUSSION

By using laser-produced X-ray pulses, this experiment shows, for the first time, the possibility of identifying material compositions of hidden objects via backscattered X-ray inspection. This system can be mounted on a mobile transporter, such as a trailer truck, equipped with an extremely short-pulse X-ray source, a primary X-ray scanner, and a high-temporal-resolution detector for the backscattered signals.

If we apply this technique for maintaining the safety of public transport facilities and protection against potential dangers, the system should be approximately 10 m from objects. In the present experiments, the distance between detector and object was 15 cm because of restrictions of the present X-ray source specification (the divergence and photon numbers) and size of the detector. According to a feasibility study,¹⁷ if we apply a pencil beam X-ray source with a narrower divergence of 3 mrad and larger photon numbers of 10^6 photons/pulse, we can extend the detection distance to 10 m. Then, by using a scintillator array detector with a diameter of 2 m located near the source, we could detect 440 photons/pulse from a 2-mm-thick aluminium container filled with 30-mm-deep water.

During these processes, primary and backscattered X-rays are attenuated in air. In the proposed inspection system, the primary X-rays have an appropriate energy range, which is from 100 keV to 1 MeV. From Eq. (5), the energy of backscattered ($\phi = \pi$) X-rays is evaluated to be between 72 keV and 204 keV. The corresponding attenuation length in air at normal conditions is $\sim 2 \times 10^{-4} \text{ cm}^{-1}$. Therefore, at a distance of 10 m, the attenuation of backscattered X-ray signals, which is stronger than that of primary X-rays, would be less than 18%. Even at this level of attenuation, the coincident technique enables us to distinguish backscattered signals from background noise. To realize a compact collimated pencil X-ray source, one possibility is inverse Compton scattering from a laser-driven electron.^{19–22} For example, when electrons with an energy of 150 MeV (Lorentz factor γ of 300) scatter a counter-propagating laser with a wavelength of $0.8 \mu\text{m}$ (corresponding photon energy ϵ_L of 1.6 eV), the resulting inverse Compton scattering light has a divergence of $1/\gamma \sim 3.3 \text{ mrad}$ and an energy of $4\gamma^2\epsilon_L \sim 558 \text{ keV}$. By using the proposed inverse Compton scattering light as a primary X-ray source, the attenuation of the primary X-ray can be maintained at 5% at a distance of 10 m. This level of

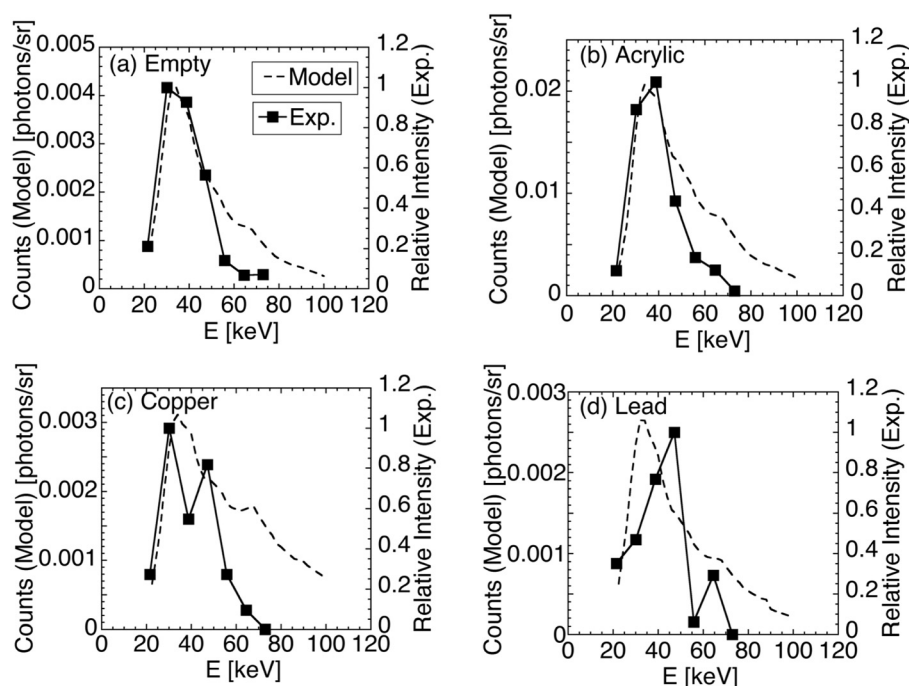


FIG. 7. Backscattered spectrum from calculation model (dashed lines) compared with experiments (solid points). (a) Empty aluminium container, (b) 30-mm-thick acrylic block, (c) 5-mm-thick copper block, (d) 1-mm-thick lead block in the 0.8-mm-thick aluminium container.

attenuation is expected to be trivial in practical applications. Therefore, this technique can be made available for low-dose inspections of human bodies, plants, and foods. By combining this pulsed X-ray source with a high-temporal-resolution detector, the system could be used for standoff inspections of structural integrity of huge objects, such as bridges and piers.

V. CONCLUSIONS

We have demonstrated standoff imaging of hidden objects by coincident measurements of primary and backscattered X-rays. A CPA laser serves as an extremely short-pulse X-ray source. Coincident measurement with primary X-rays enables a few backscattered photons to differentiate between acrylic, copper, and lead blocks inside an aluminum container. The objects modify the energy spectra of the backscattered X-rays, which can further confirm the identities of the materials. This achievement is an important step towards standoff inspection of any unknown or hidden object, and because of the compactness of the laser, the system has great potential for homeland security measures. This new standoff backscattered X-ray inspection technique may first be applied in inspecting objects suspected of being explosives or found floating at sea. In the future, the technique can be used for standoff inspection of structural integrity of huge objects, such as bridges and piers.

ACKNOWLEDGMENTS

This work was supported by Grants-in-Aid for Scientific Research from MEXT #21244088, 2008-2010 Grants of the Science Research Promotion Fund of the Promotion and Mutual Aid Corporation for Private Schools of Japan, the GPI-IHI Research Collaboration, as well as research collaboration with the ILE, Osaka University #B2-41. We wish to acknowledge the support of all the GPI staff.

- ¹Y. Glinec, J. Faure, L. Le Dain, S. Darbon, T. Hosokai, J. J. Santos, E. Lefebvre, J. P. Rousseau, F. Burgy, B. Mercier, and V. Malka, *Phys. Rev. Lett.* **94**, 025003 (2005).
- ²R. Toth, J. C. Kieffer, S. Fourmaux, T. Ozaki, and A. Krol, *Rev. Sci. Instrum.* **76**, 083701 (2005).
- ³L. M. Chen, M. Kando, J. Ma, H. Kotaki, Y. Fukuda, Y. Hayashi, I. Daito, T. Homma, K. Ogura, M. Mori, A. S. Pirozhkov, J. Koga, H. Daido, S. V. Bulanov, T. Kimura, T. Tajima, and Y. Kato, *Appl. Phys. Lett.* **90**, 211501 (2007).
- ⁴K. Takano, K. Nemoto, T. Nayuki, Y. Oishi, T. Fujii, A. Zhidkov, E. Hotta, M. Todoriki, and S. Hasegawa, *Appl. Phys. Lett.* **92**, 251502 (2008).
- ⁵S. Kneip, C. McGuffey, F. Dollar, M. S. Bloom, V. Chvykov, G. Kalintchenko, K. Krushelnick, A. Maksimchuk, S. P. D. Mangles, T. Matsuoka, Z. Najmudin, C. A. J. Palmer, J. Schreiber, W. Schumaker, A. G. R. Thomas, and V. Yanovsky, *Appl. Phys. Lett.* **99**, 093701 (2011).
- ⁶S. Fourmaux, S. Corde, K. Ta Phuoc, P. Lassonde, G. Lebrun, S. Payeur, F. Martin, S. Sebban, V. Malka, A. Rousse, and J. C. Kieffer, *Opt. Lett.* **36**, 2426 (2011).
- ⁷Y. Oishi, T. Nayuki, C. Nakajima, T. Fujii, A. Zhidkov, and K. Nemoto, *Jpn. J. Appl. Phys., Part 1* **49**, 046602 (2010).
- ⁸L. Lawson, *Mater. Eval.* **60**, 1295 (2002).
- ⁹J. S. Ryu, S. W. Park, M. S. Kim, and Y. Yi, in *Proc. 27th Int. Conf. IEEE Eng. Med. Biol. Soc.* (2005), p. 1838.
- ¹⁰R. D. Swift, *Proc. SPIE* **2936**, 124 (1997).
- ¹¹H. Kuwabara, Y. Mori, and Y. Kitagawa, *J. Plasma Fusion Res.* **3**, 003 (2008).
- ¹²Y. Mori and Y. Kitagawa, *Appl. Phys. B* **110**, 57 (2013).
- ¹³S. C. Wilks, W. L. Kruer, M. Tabak, and A. B. Langdon, *Phys. Rev. Lett.* **69**, 1383 (1992).
- ¹⁴S. Ootsuka, Y. Mori, T. Makino, M. Ohta, H. Kuwabara, and Y. Kitagawa, *Rev. Laser Eng.* **38**, 386 (2010).
- ¹⁵J. H. Hubbell, *Int. J. Appl. Radiat. Isot.* **33**, 1269 (1982).
- ¹⁶K. Fujitaka, M. Abe, and S. Abe, in *3rd Int. Symp. Adv. Nucl. Eng. Res., Global environment and Nuclear Energy* (1991), p. 76.
- ¹⁷H. Kuwabara, Ph.D. thesis, Graduate School for the Creation of New Photonics Industries, Hamamatsu, 2008.
- ¹⁸V. O. Klein and Y. Nishina, *Z. Phys.* **52**, 853 (2003).
- ¹⁹H. Schwoerer, B. Liesfeld, H.-P. Schlenvoigt, K.-U. Amthor, and R. Sauerbrey, *Phys. Rev. Lett.* **96**, 014802 (2006).
- ²⁰Y. Mori, H. Kuwabara, K. Ishii, R. Hanayama, T. Kawashima, and Y. Kitagawa, *Appl. Phys. Express* **5**, 056401 (2012).
- ²¹K. T. Phuoc, S. Corde, C. Thauray, V. Malka, A. Tafzi, J. P. Goddet, R. C. Shah, S. Sebban, and A. Rousse, *Nat. Photonics* **6**, 308 (2012).
- ²²S. Chen, N. D. Powers, I. Ghebregziabher, C. M. Maharjan, C. Liu, G. Golovin, S. Banerjee, J. Zhang, N. Cunningham, A. Moorti, S. Clarke, S. Pozzi, and D. P. Umstadter, *Phys. Rev. Lett.* **110**, 155003 (2013).